Infrared and terahertz spectrally adaptive filters based on MEMS technologies

Mariusz Martyniuk, KKMB Dilusha Silva, Hemendra Kala, Michal Zawierta, Vincent Wallace, et al.

Mariusz Martyniuk, KKMB Dilusha Silva, Hemendra Kala, Michal Zawierta, Vincent P. Wallace, Konrad Walus, Lorenzo Faraone, Ilya V. Shadrivov, "Infrared and terahertz spectrally adaptive filters based on MEMS technologies," Proc. SPIE 12425, Smart Photonic and Optoelectronic Integrated Circuits 2023, 124250H (17 March 2023); doi: 10.1117/12.2658896

Event: SPIE OPTO, 2023, San Francisco, California, United States

Infrared and terahertz spectrally adaptive filters based on MEMS technologies

Mariusz Martyniuk*[a], KKMB Dilusha Silva[a], Hemendra Kala[a], Michal Zawierta[a], Vincent P. Wallace[b], Konrad Walus[c], Lorenzo Faraone[a], Ilya V. Shadrivov[d]
[a]ARC Centre for Transformative Meta-Optical Systems, Dept. of Electrical, Electronic & Computer Engineering, The University of Western Australia, 35 Stirling Highway, Perth, WA, 6009, Australia; [b]Dept. of Physics, The University of Western Australia, 35 Stirling Highway, Perth, WA, 6009, Australia; [c]Electrical and Computer Engineering, The University of British Columbia, Vancouver, Canada; [d]Nonlinear Physics Centre, Research School of Physics and Engineering, Australian National University, Canberra, ACT 2601, Australia

ABSTRACT

Future remote imaging systems promise spectroscopic functionalities extending well beyond the visible wavelengths. This allows real-time spectral information to be gathered from multiple wavelength bands which is highly attractive for numerous remote sensing spectroscopy/imaging applications and aids target recognition. This paper briefly presents a micro-electromechanical systems (MEMS) based electrically tuneable adaptive filter technology developed for the technologically important infrared (IR) bands of the electromagnetic spectrum and reports on the progress towards extension to the significantly longer wavelength THz band. The demonstrated concepts focus on merging MEMS-enabled dynamic modulation with the spectral sensitivity and selectivity of metamaterials, as well as on the possibility of adopting the rapidly evolving 3D printing technologies.

Keywords: infrared, terahertz, microelectromechanical systems, optical device fabrication, optical filters

1. INTRODUCTION

State-of-the-art remote sensing and imaging technologies enabled by microelectromechanical system (MEMS) are currently emerging incorporating so-called multi/hyper-spectral capabilities, which allow real-time spectral information to be gathered from multiple wavelength bands. Multi/hyper-spectral imaging systems can extract spectral signatures of objects, and thus provide enhanced detection and discrimination of targets in clutter in comparison to single-band imaging systems. Usefulness of this capability in imaging systems has been well established in the atmospheric transmission windows of the SWIR (short-wavelength infrared, 1.6–2.5 µm), MWIR (mid-wavelength infrared, 3–5 µm), and LWIR (long-wavelength infrared, 8–12 µm) for a wide variety of applications, such as gas and volatile organic compound diagnostics,[1-3] mineral mapping,[4, 5] and global atmospheric temperature profile monitoring.[6, 7] Particularly attractive is also extension of wavelength discrimination beyond the infrared into much longer wavelength electromagnetic waves in the terahertz frequency range (THz, one trillion Hertz or hundreds of micrometers in wavelength). THz radiation has a particular potential to provide significant capabilities in many diversified areas. In addition to penetration through non-metallic materials, the key advantage of THz radiation is its interaction with the absorption of significantly more complex organic molecules in comparison to the IR. THz signatures allow the identification of many man-made synthetic materials through their unique absorption spectra, making it possible to distinguish for example illegal drugs and explosives from benign compounds.[8] However, the current impediment is the lack of sensitive, inexpensive and efficient terahertz devices. Significant research is required to realize components for cost-effective filtering and manipulation of THz radiation in addition to the development of THz sources and detectors.

Replacement of large optics with high-speed MEMS-tunable filters provides fundamentally low cost and small form factor delivering a highly attractive reduced size, weight and power (SWaP) solution. This is exemplified by a robust adaptive wavelength filtering technology based on MEMS-enabled electrically tunable Fabry-Pérot (FP) optical filters. An FP filter consists of two parallel mirrors separated by an optical cavity. The mirrors are typically distributed Bragg reflectors (DBR) composed of alternating quarter-wave thick layers of high-refractive-index and low-refractive-index materials. Ignoring phase changes on mirror reflection, the optical transmission of the filter is maximized at the resonant

---

*mariusz.martyniuk@uwa.edu.au; phone +61 8 6488 1905; fax +61 8 6488 1095

Smart Photonic and Optoelectronic Integrated Circuits 2023, edited by Sailing He,
Laurent Vivien, Proc. of SPIE Vol. 12425, 124250H · © 2023 SPIE
0277-786X · doi: 10.1117/12.2658896

wavelength that is exactly double the optical cavity length, when operating in first-order.[9] For other wavelengths, the optical transmission falls off rapidly away from the peak resonance value, creating a spectrally isolated transmission pass-band. Using an electrical stimulus to control the mirror separation, the transmission pass-band can be swept over a range of wavelengths, realizing an electrically tunable optical filter. The critical spectral parameters of a tunable FP filter include the wavelength tuning range, the peak transmission, the full-width at half-maximum (FWHM) of the transmission peak, the out-of-band rejection (transmission maximum-to-minimum ratio), and the pixel-to-pixel transmission peak wavelength uniformity across the optical imaging area.

In this contribution, we note the review[10] on the adoption of the FP filter approach for applications in the IR spectrum and briefly present the MEMS-based FP IR filter designs being realized at The University of Western Australia (UWA) since this is the focus of Ref.[11] Subsequently, we highlight that direct extension of wavelength discrimination based on Fabry-Pérot concept adopted in the IR to the THz band is made impractical for MEMS technologies by the requirement to reach ¼ wavelength design thicknesses for mirror layers. This necessitates the use of thin films of thicknesses approaching 50-100µm, and even thicker sacrificial layers which can be associated with prohibitively long deposition times and the resulting overall device thickness can extend beyond acceptable limits for some applications. Consequently, shifting to the THz band we report on progress of using approaches alternative to the Fabry-Pérot concept; focusing on merging MEMS-enabled dynamic modulation with the spectral sensitivity and selectivity of metamaterials, as well as the rapidly evolving 3D printing technology.

2. SPECTRALLY ADAPTIVE INFRARED FP FILTERS

The FP MEMS technologies[12] at UWA were mainly developed according two distinct structural designs that are depicted in Figure 1. In both cases an underlying IR detector (not shown) senses only photons that have been discriminated for a particular wavelength pass-band by a tuneable FP interferometric filter. In the instance of the MEMS design depicted in Figure 1 (a), the FP cavity is formed between two Bragg reflectors realized using alternating layers of high and low refractive index materials, where best performance is achieved when the contrast between the values of the refractive index is maximized. The discriminated wavelength is determined by the spacing between the top and bottom reflectors. The top reflector is supported by a suspended SiN_x membrane connected via tethers to four fixed-fixed beam actuators. The role of the tethers is to reduce any transverse load on the beams arising from net tensile stresses in the centrally

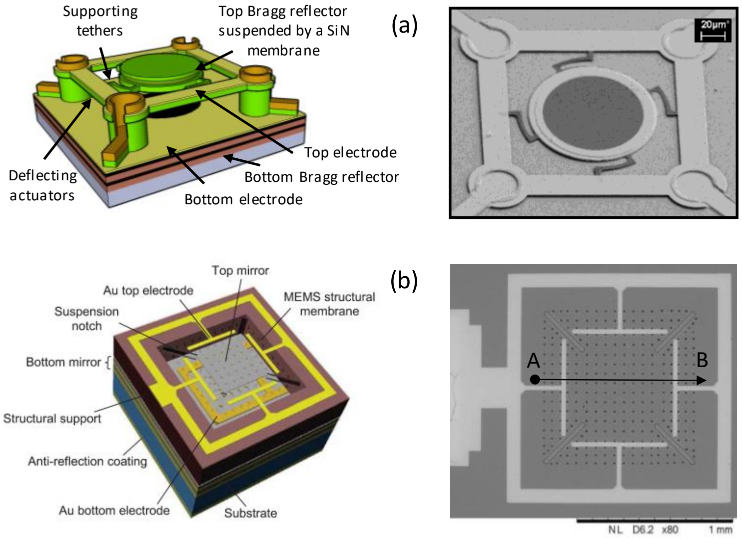

Fig. 1. Schematic three dimensional illustrations (left) and scanning electron micrographs (right) presenting two distinct conceptual designs of micro-machined Fabry-Perot (FP) filters fabricated at UWA. An underlying IR detector (not shown) senses only photons that have been discriminated for a particular wavelength pass band by a tuneable FP interferometric cavity formed between two mirrors. In both cases the top mirror is supported by a suspended membrane and electrostatic actuation is used to vary its position. This allows electronic control of the cavity length and provides wavelength tuneability. The top MEMS structural membrane in (b) is drawn semitransparent to allow the bottom electrode layout to be visible. Please note that the scale bars for the two scanning electron micrographs are vastly different.

suspended mirror. Electrostatic actuation is used to attract the top electrodes to the substrate and vary the position of the top reflector, thus providing a means of controlling the cavity length and resulting in wavelength tuneability.

The main feature motivating the use of the MEMS design depicted schematically in Figure 1 (a) is its effectiveness in de-coupling of the mechanical actuation and associated requirements on the actuating geometry and materials, from the optical requirements imposed on the cavity. Effectively, one can attempt to separately optimize the mechanical and optical performance of the device. A significant advantage of this structure is the ability to use strain stiffening concepts in fixed-fixed beam actuators to extend the tuning range of MEMS to beyond 1/3 of the unactuated suspension gap that is a common limitation of MEMS parallel-plate electrostatic actuators due to uncontrolled snap-down.[13] This design has been used previously to monolithically fabricate FP filters directly on top of pre-fabricated HgCdTe IR detectors,[14, 15] using MEMS fabrication processes with a maximum processing temperature of 125°C due to the temperature sensitivity of the HgCdTe substrate.[16] This approach is also well suited to concepts integrating separately controlled filters optically in front of each individual pixel of an imaging array. However, the geometry of this design is particularly sensitive to any stress imbalance resulting in a relatively narrow window for processing tolerances. Issues relating to thin film stress and stability become extensively relevant.[17-21]

In comparison to the geometry depicted in Figure 1 (a), the MEMS design presented schematically in Figure 1 (b) is significantly more robust to variations in thin film stress and fabrication tolerances. In this approach the top movable mirror is located in the center of a suspended MEMS structural membrane, which extends all the way to the outer perimeter of the solid structural support. The resulting advantage of this MEMS design is that any tensile stress inherent in the thin film will tend to stretch the whole suspended membrane, thus aiding in flattening the central mirror and eliminating the need for any stress management. Four driving electrodes are deposited on the MEMS structural membrane around the central mirror which, in combination with the underlying bottom electrode, move the top mirror

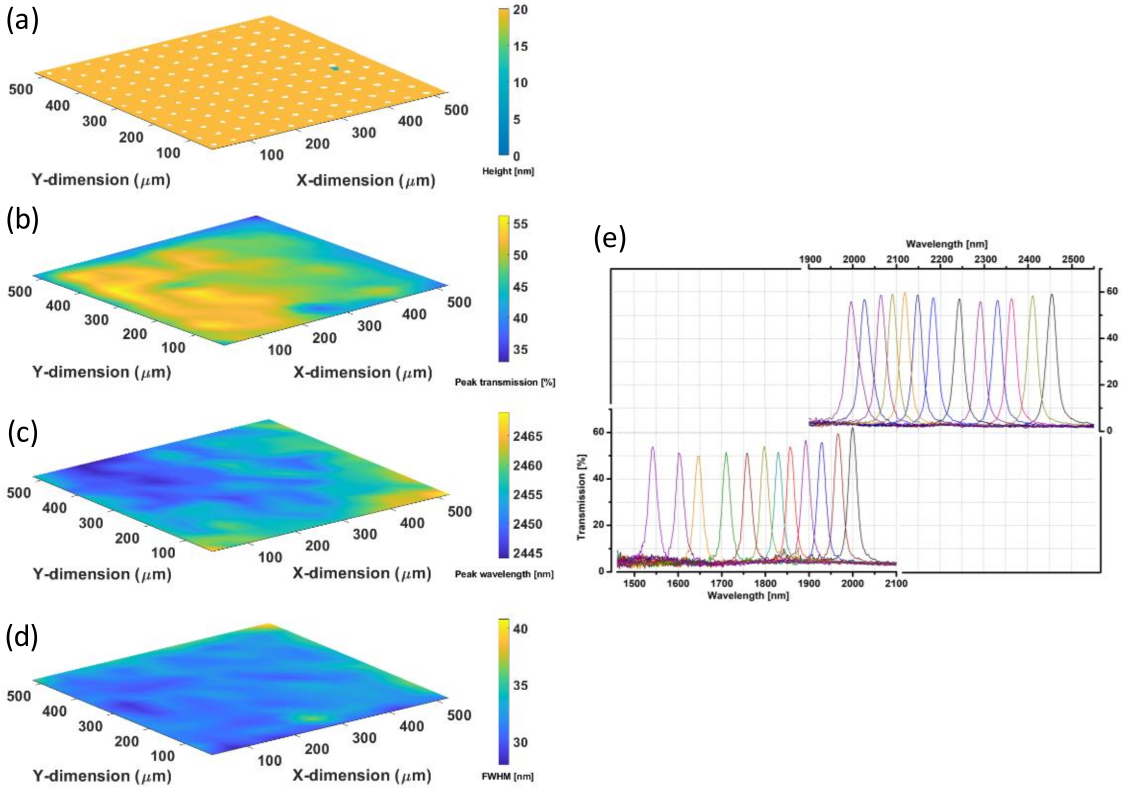

Fig. 2. (a) Colour maps presenting the achieved spatial uniformities in (a) surface profile of the unactuated FP cavity suspended top mirror, (b) total percentage of peak transmission, as well as (c) the transmitted peak centre wavelength and (d) FWHM values over 500 µm × 500 µm optical aperture area of the realised FP filter. (e) Experimentally measured transmission spectra for two realised devices of different FP cavity gaps resulting in continuous wavelength tuning ranges that overlap each other in order to cover the full SWIR spectral range.[12]

closer to the bottom mirror during electrostatic actuation. Diagonally arranged notches at the corners of the structural membrane serve to release the convergence of tensile stress from two orthogonal directions, allowing freestanding membrane actuation without causing stress induced distortion in the central mirror. These notches also reduce the spring stiffness of the membrane and thus allow low-voltage actuation. An array of 5-μm diameter holes perforated in the membrane facilitates the sacrificial layer etching process. The optical path of the etch hole array is masked by an array of gold micropatterns deposited on the bottom mirror.

Both structures presented in Figure 1 can employ a gold optical shield layer with a central window matched to the mirror dimension deposited on the backside of the substrate in order to block stray light from outside of the mirror area (not shown). In addition, a quarter-wavelength thick anti-reflection coating can be deposited on the backside of the substrate to reduce backside reflections at the substrate-air interface, thus improving the optical transmission of the filter.

Figure 2 presents exemplar characteristics of a tunable optical filter realized according to the structure shown in Figure 1 (b) which has been combined with a broadband infrared detector to yield an on-chip SWIR spectrometer for deployment on field portable platforms.[22] For this application, the suspended mirror consisted of symmetrical Si-SiO_x-Si quarter-wavelength-thick layers in order to achieve a narrower FWHM. Figure 2 (a) shows the surface map of an unactuated suspended mirror obtained by white light optical profilometry. The demonstrated uniformity in mirror flatness over the optical area allowed for the peak transmission to remain near or above 50% over the full aperture apart from a very narrow region around the mirror periphery, as shown by the colour map presented in Figure 2 (b). The resulting spatial uniformity of the centre wavelength and FWHM of the transmitted peak is validated to be within single nanometers and shown using the colour maps in Figure 2 (c) and (d), respectively. Figure 2 (e) shows the experimentally measured transmission spectra for two devices with two different FP cavity gaps designed to achieve continuous tuning in the SWIR ranges of 2,000-2,450 nm (see upper plot in Figure 2 (e)) and 1,550- 2,000 nm (see lower plot in Figure 2 (e)). The narrowness of the FWHM was achieved at the range of 30-35 nm by adopting the tunability of the 2nd order peak transmission, which limited the free-spectral-range of SWIR wavelength tuning to about 450 nm.

3. METAMATERIAL-ENHANCED SPECTRALLY ADAPTIVE TERAHERTZ FILTERS

The alternative approach based on harnessing the emerging concepts of metamaterials and metasurfaces can open unprecedented possibilities in manipulating electromagnetic waves at the subwavelength scale.[23, 24] This possibility is enabled by the strongly localized resonances of the building blocks, 'meta-atoms', which offer new degrees of freedom in controlling not only the electric but also the magnetic component of waves, achieving electromagnetic properties unavailable with naturally occurring materials. Metamaterials are engineered materials consisting of sub-wavelength sized 'meta-atoms' formed into a regular array. Whereas in normal materials the unit structural elements are atoms, molecules or ions, in metamaterials they are meta-atoms - mesoscopic elements with shapes engineered to achieve desired properties. The shape of a split-ring[25] is a common example of such resonant meta-atoms which are much smaller than their resonant wavelength. If these meta-atoms are small enough compared to the wavelength, then a large array of them can be modelled as an effective medium, with effective permittivity or permeability. This is analogous to natural materials, which have permittivity and permeability derived from the dipole response of their atoms; however,

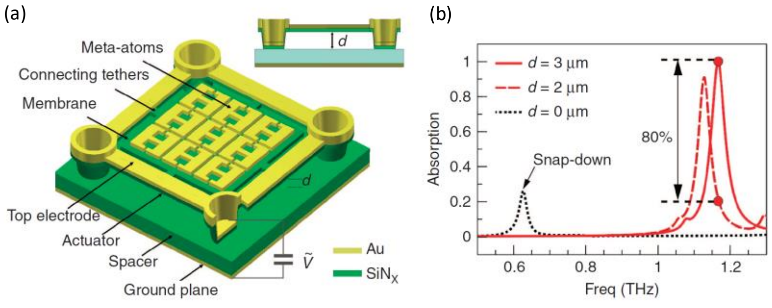

Fig. 3. (a) Schematic of the unit cell of the THz absorber based on a suspended SiN_x membrane supporting an array of meta-atoms. The vertical distance between the meta-atoms and the ground plane is tuned electrostatically enabling spectral discrimination. The shown element thicknesses are not to scale. (b) Simulated absorption spectra for different membrane suspension heights; d =3 μm and d =0 μm correspond to the undeflected and snapped-down configurations, respectively. At the threshold of snap-down (d =2 μm), absorption changes by 80% at the initial resonant frequency of approximately 1.168 THz (marked by red circles).[28]

the electric and magnetic responses of meta-atoms can be tailored and can achieve very unusual values. As a result, the electromagnetic properties of these meta-atoms can be very different from the materials from which they are composed, and can even exhibit counter-intuitive physical regimes.

The resonant nature of metamaterials means that they are well suited to provide narrow-band spectral discrimination. MEMS approaches are perfectly suited to modify the arrangement of meta-atoms and provide in a controlled fashion tunable spectral selectivity. The anisotropy of metamaterials can be significantly modified by *lateral* manipulation of the lattice of elements,[26] as well as by actuation in the direction *normal* to the metamaterial layers showing the potential to achieve much stronger tunability.[27]

In contrast to our work on FP filters operating within the IR bands which were always designed to perform filtering in transmission mode, THz structures were developed to operate and be characterized in reflection mode. Based on the MEMS design depicted in Fig. 1 (a), the unit cell of the tunable THz wavelength discriminating structure is shown schematically in Fig. 3 (a). It consists of a 200-nm-thick gold ground plane, a 2-μm-thick silicon nitride spacer layer, and an overlying matrix of meta-atoms suspended above the silicon nitride layer by a controllable distance d. The unit cell size was adopted to be 180 × 180 μm and contained 9 coupled gold meta-atoms supported by a freestanding silicon nitride square membrane with lateral dimensions of 140 μm × 140 μm and 200 nm in thickness. In order for diffraction effects not to complicate the design and characterization it was desired for the geometry of the unit cell to remain subwavelength in size relative to the resonance wavelength. The use of silicon nitride for the membrane and spacer layers was crucial for maintaining small footprint and thickness of the absorber due to its relatively high permittivity ($\varepsilon_{\mathrm{SiNx}} \approx 7$). The freestanding membrane was tethered to four symmetric micro-bridge actuators supported by four posts in a square arrangement. At rest the suspension height of the membrane was $d = 3$ μm and was tuned electrostatically by attracting the silicon nitride micro-bridge actuators over-coated with top gold electrodes to the gold ground plane, which also performed the function of a bottom electrode.

Fig. 3 (b) presents the simulated THz absorption spectra for an exemplar device indicating that when the membrane is in the unactuated rest position ($d = 3$ μm) the resonant frequency of perfect absorption is ~1.168 THz (>99%), which corresponds to a free space wavelength of ~46 times greater than the thickness of the device (5.6 μm, measured between the ground plane and the meta-atom layer). The simulated resonance peak has a FWHM of ~47 GHz ($Q \approx 24$) and when the membrane is actuated down by 1 μm ($d = 2$ μm, which corresponds to the on-set of snap-down), the resonance peak shifts by ~40 GHz with a notable change in absorption from nearly 100% to ~20% being expected at the original frequency of resonance of 1.168 THz. When the membrane is further actuated to the snapped-down position (d=0 μm), resonance can shift by more than 580 GHz, and near-perfect modulation of absorption is predicted as shown in Fig. 3 (b).

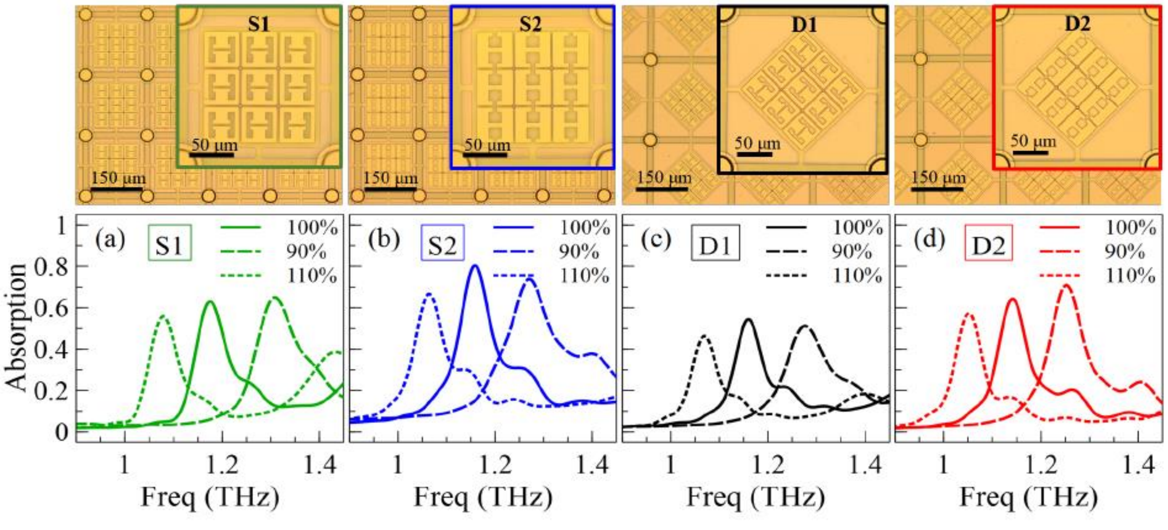

Fig. 4. Microscope photographs and the measured THz absorption spectra of the fabricated MEMS arrays. Two designs of meta-atoms based on electric split-ring resonator (denoted as ‘1’ and ‘2’) were fabricated and hybridized with a square and/or diamond supporting membrane geometry (denoted as ‘S’ and ‘D’, respectively). Spectra were also measured for devices fabricated with geometry scaled by 90% and 110% showing that the spectral position of the absorption peak can be controlled by the relative size of the meta-atoms. The photographs correspond to the 100% footprint size design.[28]

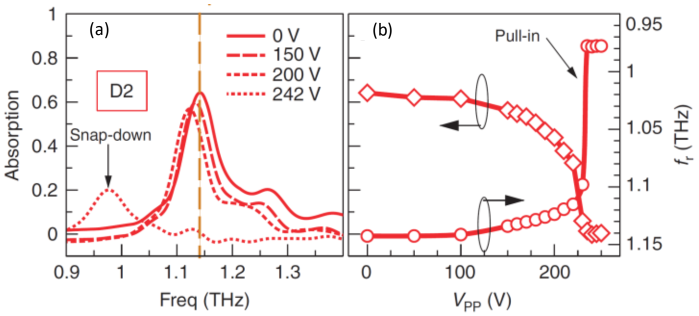

Fig. 5. (a) Measured THz absorption spectra for different actuation peak-to-peak voltages V_{pp} of an exemplar device that was driven to snap-down position (see spectrum for 242 V). For clarity, only four spectra are shown. (b) The corresponding absorption (diamond symbols) measured at the original resonant frequency for the unactuated device (indicated by the vertical line in (a)) is plotted on a common LHS axis, and the change of the resonant frequency f_r (circle symbols) is plotted on the RHS axis in (b).[28]

Two different types of meta-atoms based on electric split-ring resonators (denoted as ‘1’ and ‘2’, according to the number of gaps in the meta-atoms) were fabricated and hybridized with a square and/or diamond supporting membrane geometry. Fig. 4 shows the top-view micrographs of the realized structures, where ‘S’ and ‘D’ denote the square and diamond geometries of the supporting membranes, respectively. Arrays of the unit cells presented in Fig. 4 were fabricated extending to nominal areas of 5 mm × 5 mm and 10 mm × 10 mm to facilitate characterization with a THz beam wider than the size of individual unit cells. Fig. 4 shows the post-fabrication measured absorption spectra for the four presented designs in the static unactuated state, which were found to be in general agreement with simulated predictions.[28] Peak absorption levels were found to reach 80%. Meta-atom size tunability was studied by fabricating and characterizing arrays with meta-atom sizes 90% and 110% of the original unit cell designs, and as shown in Fig. 4 their corresponding resonances shifted by approximately ± 10%, respectively, without a significant change in absorption.

Fig. 5 (a) presents the measured absorption spectra for an exemplar electromechanically actuated device that was driven to snap-down position (see spectrum for 242 V in Fig. 5 (a)). A reasonably large resonance shift can be observed in Fig. 5 (a) as the suspended membrane approached the threshold of snap-down (~30 GHz or ~38% of the resonance linewidth). Maximum modulation was observed for the device snapped-down state (see spectrum for 242 V in Fig. 5 (a)) where the resonance shifts by 165 GHz (~206% of the resonance linewidth or ~14.4% of initial resonance wavelength) and a change of absolute absorption of up to 65% is achieved. This shift in resonance of 165 GHz corresponds to ~50 μm in units of wavelength and is unprecedented in comparison to tuning ranges attained with MEMS-based FP filters in the IR spectral bands. Furthermore, in comparison to a typical wavelength associated with THz radiation (~300 μm), merging MEMS with the concepts of optical metamaterials allowed realisation of ultrathin (~1/50 of the working wavelength) tunable THz absorbers while removing the requirement to reach ¼ wavelength design thicknesses for DBR mirror layers, which becomes a struggle for MEMS micromachining technologies since the deposition times to realize such thick films can become prohibitively long.

4. 3D-PRINTED FP FILTERS FOR TERAHERTZ SPECTRAL RANGE

In the THz band the requirement to reach the optical ¼ wavelength design layer thicknesses, which can extend to well beyond 100 μm and while being unattractive from the MEMS micromachining point of view can readily be achieved with modern 3D printing technologies. Being motivated by harnessing the benefits of 3D printing for MEMS fabrication in terms of versatility and low production costs, 3D printing was performed using polylactic acid (PLA) and an Ender FDM 3D printer (3D Technology Co., Ltd, Shenzhen, China; considered one of the most common printers at an affordable cost) to realise mirrors consisting of single and multiple 3D printed PLA layers separated by predetermined air gaps.[29] The PLA layers used to form the filters were printed with individual thicknesses of 116 ± 5 μm. This thickness corresponds to the minimum PLA layer thickness that was consistently achievable with the used apparatus. The individual 3D printed layers supported by thicker outer rings were used to construct two distinct series of devices, referred to in this paper as α-series and β-series. The α-series FP filters were formed between two 116 μm thick PLA reflectors separated by a suitable air gap (PLA-air-PLA). Fig. 6 (b) schematically shows the three-dimensional expanded and cross-sectional views depicting the construction of α-series devices. These devices consisted of three different designs in which the air gap between the PLA reflectors was 330 μm (referred to as α-330), 430 μm (α-430) and 530 μm

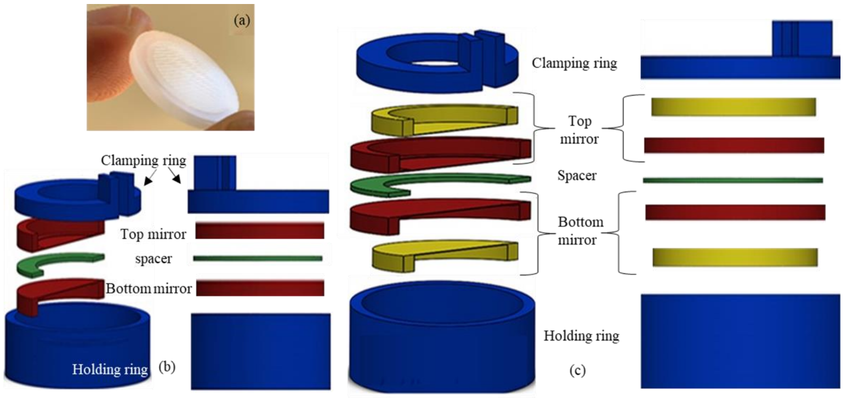

Fig. 6. (a) Photograph of the finger-held 3D printed PLA reflector used in the construction of the FP filter prototype. (b) Schematic illustrating a 3D-view as well as a cross-sectional view of stackable un-assembled α-series 3D-printed Fabry-Pérot filter where the FP cavity is formed by two single 116 µm thick PLA layers, and (c) schematic illustrating a 3D view as well as a cross-sectional view of stackable un-assembled β-series devices where the FP cavity is formed between two Distributed Bragg Reflectors (DBRs) each formed by a pair of 116 µm thick PLA layers separated by a 116 µm air gap which was pre-defined by a step noticeable in the larger (red) ring. The thickness of the spacer ring defines the central air gap forming the FP cavity in both α-series and β-series devices.[29]

(α-530). PLA spacing rings of various thicknesses (330 µm, 430 µm and 530 µm) were designed and printed to establish the air cavity between the PLA reflectors. Clamping and holding rings helped to retain the air cavity between the two individual PLA reflectors and the formed filter stack. The PLA rings defined the optical aperture with inner/outer diameter of 15 mm/18 mm. The thicknesses of the PLA reflectors forming the FP filters and the PLA spacers were confirmed via digital micrometre measurements to have an accuracy of ±5 µm.

The concept adapted for the realisation of β-series FP filters is presented in Fig. 6 (c). In contrast to α-series devices, which used single PLA layers as reflectors, β-series devices used a 3-layer structure in which each consisted of two PLA layers separated by a 116 µm air gap. This is the concept of a 3-layer DBR mirror formed by the refractive index contrast between the PLA-air-PLA layers. The intra-DBR air gap was facilitated by printing a 116 µm high step in the outer supporting ring, which serves as a hard stop and separator between the two PLA layers to form the 3-layer DBR.

This intra-mirror air gap within the DBRs is kept constant for all β-series devices. The FP main cavity for the β-series devices was created by an air gap between two identical DBRs. The β-series consisted of three devices where the air gap between the DBRs was designed to be 330 µm (referred to as β-330), 430 µm (β-430) and 530 µm (β-530). Like the α-series, PLA spacer rings of a pre-defined thickness (330 µm, 430 µm and 530 µm) were printed to establish the main air cavity. The holding ring design ensured the individual layers were not compressed and that all the air gaps between the PLA layers maintained their integrity.

A Terahertz time-domain spectroscopy system (TeraPulse4000, Cambridge, UK) was used to characterise the performance of the fabricated filter stacks. The measured transmittance spectra of α-series FP filters formed by pairs of single PLA layer reflectors separated by a main air cavity of 330 µm, 430 µm, and 530 µm are shown in Fig. 7, which also includes simulated transmittance spectra predicted analytically using optical transfer-matrix methods to estimate the frequency-dependent transmission of a thin-film stack.[30] The input parameters to the model were the measured physical parameters of individual filter components, including PLA layer thickness, refractive index, absorption coefficient, as well as the main FP cavity and intra-DBR air gaps. It can be observed that the measured results are in good agreement with the calculated response irrespective of the main filter cavity. First-order transmission peaks can be observed for each of the three filters in the frequency range of 0.33 THz – 0.43 THz, whereas the second-order transmission peaks were observed in the range of 0.56 THz – 0.71 THz. As expected, the wavelength positions of the transmission peaks within each optical order are positively correlated with the extent of the gap between top and bottom reflectors. Consistently for all filters, the magnitudes of the first order transmission peaks are near 90% or greater, and the magnitudes of the second-order transmission peaks are near 80% or greater.

For the α-430 filter, the central frequencies of the first and second-order transmission peaks are observed to be located at frequencies of 0.36 THz and 0.61 THz, respectively. FWHMs for the first and second-order transmission peaks were estimated as 0.1 THz and 0.11 THz, respectively. The free spectral range (FSR), which corresponds to the wavelength

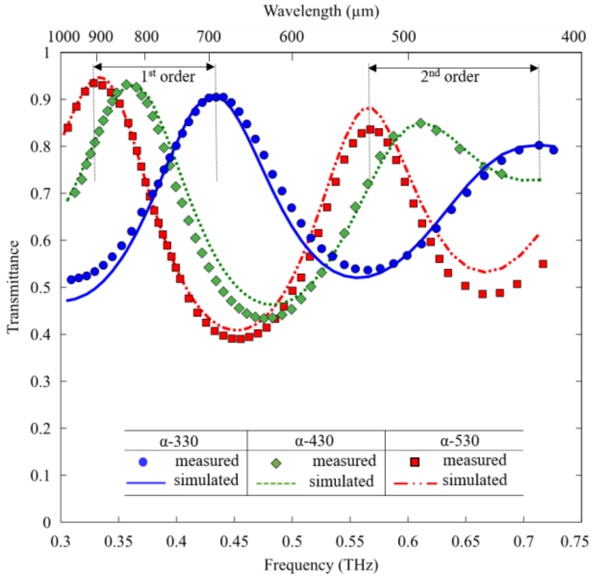

Fig. 7. Experimentally measured (data points) and simulated (lines) transmittance spectra for α-series FP filters formed by a pair of single PLA layer reflectors separated by an air gap of 330 μm (blue dots and solid blue line), 430 μm (green diamond and green dashed line), and 530 μm (red square and red dash-dot line).[29]

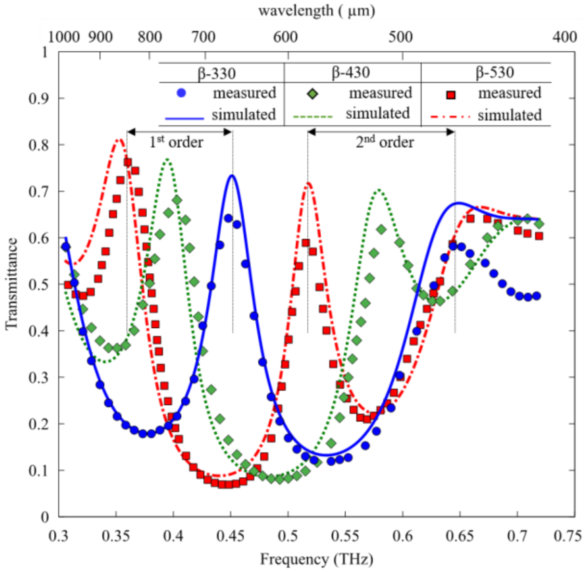

Fig. 8. Experimentally measured (data points) and simulated (lines) transmittance spectra for β-series FP filters formed by a pair of two PLA-air-PLA DBR reflectors separated by an air gap of 330 μm (blue dots and solid blue line), 430 μm (green diamond and green dashed line), and 530 μm (red square and red dash-dot line).[29]

separation between the 1st and 2nd order peaks, was 0.25 THz. Similar observations can be made in Fig. 7 for α-330 and α-530 filters.

The measured and simulated transmittance spectra of β-series FP filters are shown in Fig. 8. This series consisted of devices formed by DBR pairs separated by main air cavities of 330 μm, 430 μm, and 530 μm. It can be ascertained that the measured responses agree well with simulations in the investigated frequency range of 0.3 THz – 0.75 THz. First-order transmission peaks can be observed for each of the three filters in the frequency range of 0.36 THz – 0.45 THz, whereas the second-order transmission peaks were observed in the range of 0.52 THz – 0.64 THz. Consistently for all β-series devices, the magnitudes of the first-order maximum transmission peaks were observed to be 64% –76%, and for the second-order transmission peaks to be around 58% or greater. For the β-430 filter, the FWHMs of the 1st and 2nd order peaks were estimated to be 0.039 THz and 0.043 THz, respectively, and the free spectral range was found to be 0.18 THz. Similar observations can be made for other filters in the β series.

The reflectivity of mirrors used to construct the devices was the most relevant parameter that results in the differences in the observed performance between the α and β series filters. The reflectance for the single-layer PLA mirror was found to be below 20% across the investigated frequency range of 0.30 THz – 0.75 THz and for the PLA-air-PLA DBR to reach a peak value of 50% at a frequency of 0.46 THz.[29] Nevertheless, the relatively poor reflectivity of below 20% for single PLA layer mirrors that were used to construct the α-series devices were adequate to achieve FP filter peak transmission of 90-94% (see Fig. 7). In this aspect, α-series devices outperformed the β series. However, the α-series filters, in comparison to the β series, were observed to be characterised by reduced spectral performance, with broader transmission peaks and poor out-of-band rejection (transmission maximum-to-minimum ratio). For the β-series filters presented in Fig. 8, the measured transmission peaks were observed to be characterized by FWHM values of 40-50 GHz, with out-of-band rejection ratios approaching 10:1. This level of spectral performance for the β series filters has been achieved with a signal peak transmission well above 50%, which may be the necessary lower bound for sufficient optical throughput to attain a satisfactory system signal-to-noise ratio.[31]

5. CONCLUSION

This review has presented the progress towards extension of adaptive wavelength discrimination typically realized using MEMS-based FP concepts from the IR spectral band to the significantly longer wavelength THz band. It has been shown that in comparison to a typical wavelength associated with THz radiation (~300 μm), merging MEMS with the concepts of optical metamaterials allowed realisation of ultrathin (~1/50 of the working wavelength) tunable THz absorbers while removing the need to reach ¼ wavelength design thicknesses for mirror layers, which become a struggle for MEMS micromachining technologies since the deposition times to realize such thick films can become prohibitively long. Furthermore, adoption of the rapidly evolving 3D printing technology for fabrication of THz FP filters has shown that despite relatively poor optical performance of individual 3D-printed PLA layers, the demonstrated filter characteristics can be adequate for many applications harnessing the terahertz spectral range. The impact of a viable 3D printing approach delivering devices at trivial cost levels in comparison to the current market alternatives cannot be overemphasized as it has the potential to revolutionize this landscape and bring on-demand desktop-MEMS development within the reach of common home-based enthusiasts.

ACKNOWLEDGEMENTS

This work was supported in part by the facilities of the Western Australian node of the NCRIS-enabled Australian National Fabrication Facility (ANFF), a company established under the National Collaborative Research Infrastructure Strategy (NCRIS) to provide nano and micro-fabrication facilities for Australia's researchers and support from the Western Australian Government's Department of Jobs, Tourism, Science and Innovation. This research was supported financially by Australian Research Council. The authors also thankfully acknowledge the facilities, and the scientific and technical assistance of the Centre for Microscopy, Characterisation & Analysis (CMCA); and The University of Western Australia.

REFERENCES

[1] Zhang, L. and G.W. Small, "Automated Detection of Chemical Vapors by Pattern Recognition Analysis of Passive Multispectral Infrared Remote Sensing Imaging Data," *Applied Spectroscopy* 56(8), p. 1082-1093 (2002)

[2] Teggi, S., M. Bogliolo, M. Buongiorno, S. Pugnaghi, and A. Sterni, "Evaluation of SO2 emission from Mount Etna using diurnal and nocturnal multispectral IR and visible imaging spectrometer thermal IR remote sensing images and radiative transfer models," *Journal of Geophysical Research: Solid Earth* 104(B9), p. 20069-20079 (1999)

[3] Wabomba, M.J., Y. Sulub, and G.W. Small, "Remote detection of volatile organic compounds by passive multispectral infrared imaging measurements," *Applied spectroscopy* 61(4), p. 349-358 (2007)

[4] Kahle, A.B. and A.F. Goetz, "Mineralogic information from a new airborne thermal infrared multispectral scanner," *Science* 222(4619), p. 24-27 (1983)

[5] Vaughan, R.G., S.J. Hook, W.M. Calvin, and J.V. Taranik, "Surface mineral mapping at Steamboat Springs, Nevada, USA, with multi-wavelength thermal infrared images," *Remote Sensing of Environment* 99(1-2), p. 140-158 (2005)

[6] Clodius, W.B., C. Borel, L. Balick, and S.J. Hook. "Validation of the MTI water surface temperature retrieval algorithms," *IEEE International Geoscience and Remote Sensing Symposium*: IEEE, p. 30-32 (2002)

[7] Rodger, A.P., L.K. Balick, and W.B. Clodius, "The performance of the multispectral thermal imager (MTI) surface temperature retrieval algorithm at three sites," *IEEE transactions on geoscience and remote sensing* 43(3), p. 658-665 (2005)

[8] Davies, A.G., A.D. Burnett, W. Fan, E.H. Linfield, and J.E. Cunningham, "Terahertz spectroscopy of explosives and drugs," *Materials today* 11(3), p. 18-26 (2008)

[9] Stupar, P., R. Borwick, J. DeNatale, P. Kobrin, and W. Gunning. "MEMS tunable Fabry-Perot filters with thick, two sided optical coatings," *TRANSDUCERS 2009-2009 International Solid-State Sensors, Actuators and Microsystems Conference*: IEEE, p. 1357-1360 (2009)

[10] Ebermann, M., N. Neumann, K. Hiller, M. Seifert, M. Meinig, and S. Kurth, *Tunable MEMS Fabry-Pérot filters for infrared microspectrometers: a review*, Proc. SPIE, Vol. 9760, 97600H (2016).

[11] Martyniuk, M., K.D. Silva, G. Putrino, H. Kala, D.K. Tripathi, and L. Faraone. "MEMS for multispectral imaging," *Smart Photonic and Optoelectronic Integrated Circuits 2022*: SPIE, p. 22-31 (2022)

[12] Martyniuk, M., K.D. Silva, G. Putrino, H. Kala, D.K. Tripathi, G. Singh Gill, and L. Faraone, "Optical Microelectromechanical Systems Technologies for Spectrally Adaptive Sensing and Imaging," *Advanced Functional Materials*, p. 2103153 (2021)

[13] Milne, J.S., J.M. Dell, A.J. Keating, and L. Faraone, "Widely tunable MEMS-based Fabry–Perot filter," *Journal of microelectromechanical systems* 18(4), p. 905-913 (2009)

[14] Musca, C., J. Antoszewski, K. Winchester, A. Keating, T. Nguyen, K. Silva, J. Dell, L. Faraone, P. Mitra, and J. Beck, "Monolithic integration of an infrared photon detector with a MEMS-based tunable filter," *IEEE electron device letters* 26(12), p. 888-890 (2005)

[15] Antoszewski, J., K.J. Winchester, T. Nguyen, A.J. Keating, K.D. Silva, C.A. Musca, J.M. Dell, and L. Faraone, "Materials and processes for MEMS-based infrared microspectrometer integrated on HgCdTe detector," *IEEE Journal of selected topics in quantum electronics* 14(4), p. 1031-1041 (2008)

[16] Martyniuk, M., "Low-temperature micro-opto-electro-mechanical technologies for temperature sensitive substrates," University of Western Australia (2006)

[17] Martyniuk, M., J. Antoszewski, C. Musca, J. Dell, and L. Faraone, "Stress in low-temperature plasma enhanced chemical vapour deposited silicon nitride thin films," *Smart Materials and Structures* 15(1), p. S29 (2005)

[18] Martyniuk, M., C.A. Musca, J.M. Dell, R.G. Elliman, and L. Faraone, "Elasto-plastic characterisation of low-temperature plasma-deposited silicon nitride thin films using nanoindentation," *International Journal of Surface Science and Engineering* 3(1-2), p. 3-22 (2009)

[19] Martyniuk, M., C. Musca, J. Dell, and L. Faraone, "Long-term environmental stability of residual stress of SiNx, SiOx, and Ge thin films prepared at low temperatures," *Materials Science and Engineering: B* 163(1), p. 26-30 (2009)

[20] Martyniuk, M., J. Antoszewski, C. Musca, J. Dell, and L. Faraone, "Environmental stability and cryogenic thermal cycling of low-temperature plasma-deposited silicon nitride thin films," *Journal of applied physics* 99(5), p. 053519 (2006)

[21] Martyniuk, M., J. Antoszewski, C. Musca, J. Dell, and L. Faraone, "Dielectric thin films for MEMS-based optical sensors," *Microelectronics Reliability* 47(4-5), p. 733-738 (2007)

[22] Silva, D., D. Tripthi, H. Kala, M. Zawierta, J. Silva, G. Putrino, M. Martyniuk, J. Antoszewski, A. Keating, and L. Faraone. "MEMS-based lightweight solutions for infrared spectral sensing and imaging," *19th meeting of the International Council for NIR Spectroscopy (ICNIRS)* Brisbane, (2019)

[23] Pendry, J.B., D. Schurig, and D.R. Smith, "Controlling electromagnetic fields," *science* 312(5781), p. 1780-1782 (2006)

[24] Smith, D.R. and N. Kroll, "Negative refractive index in left-handed materials," *Physical review letters* 85(14), p. 2933 (2000)

[25] Watts, C.M., X. Liu, and W.J. Padilla, "Metamaterial electromagnetic wave absorbers," *Advanced materials* 24(23), p. OP98-OP120 (2012)

[26] Costa, F., S. Genovesi, A. Monorchio, and G. Manara, "A circuit-based model for the interpretation of perfect metamaterial absorbers," *IEEE Transactions on Antennas and Propagation* 61(3), p. 1201-1209 (2012)

[27] Chen, H.-T., "Interference theory of metamaterial perfect absorbers," *Optics express* 20(7), p. 7165-7172 (2012)

[28] Liu, M., M. Susli, D. Silva, G. Putrino, H. Kala, S. Fan, M. Cole, L. Faraone, V.P. Wallace, W.J. Padilla, D.A. Powell, I.V. Shadrivov, and M. Martyniuk, "Ultrathin tunable terahertz absorber based on MEMS-driven metamaterial," *Microsystems & Nanoengineering* 3(1), p. 17033 (2017)

[29] Revuri, P.K., K. Walus, V.P. Wallace, K. Silva, A. Keating, L. Faraone, and M. Martyniuk, "3D Printed Fabry–Pérot Filters for Terahertz Spectral Range," *Journal of Infrared, Millimeter, and Terahertz Waves*, p. 1-15 (2022)

[30] MacLeod, H., "Thin Film Optical Filters," Inst. of Physics Publishing, London (2001)

[31] Mao, H., K.K.M.B.D. Silva, M. Martyniuk, J. Antoszewski, J. Bumgarner, B.D. Nener, J.M. Dell, and L. Faraone, "MEMS-Based Tunable Fabry-Perot Filters for Adaptive Multispectral Thermal Imaging," *Journal of Microelectromechanical Systems* 25(1), p. 227-235 (2016)